Supporting Information

Oscar et al. 10.1073/pnas.1403712111

SI Text

SI Materials and Methods

Protein Sample Preparation. To purify the green-blue dual-emission genetically encoded Ca^{2+} sensor for optical imaging (GEM-GECO1) for in vitro spectroscopic characterization, electrocompetent *Escherichia coli* DH10B cells was transformed with the pTorPE plasmid harboring 6-histidine tagged GEM-GECO1 (1). Following selection on Lysogeny broth (LB)/ampicillin (200 μg/mL; Sigma), single colonies were picked and used to inoculate 4 mL LB medium (200 μg/mL ampicillin only). Bacterial subcultures were shaken at 250 rpm and allowed to grow overnight at 37 °C. The next day, 1 mL of bacterial subculture was added into 1 L of a modified terrific broth (TB) rich medium (1 L sterilized medium contains 20 g LB mix, 14 g trytone, 7 g yeast extract, 9.2 g K_2HPO_4, 2.2 g KH_2PO_4, and 8 mL glycerol, pH adjusted to 7.20) supplemented with 0.0020% (wt/vol) L-arabinose (Alfa Aesar). The cultures were shaken at 250 rpm and inoculated at 30 °C for 2 d. Bacteria were harvested by centrifugation (6,000 g for 5 min), resuspended in 30 mM Tris · HCl buffer (pH 7.4), lysed by French press, and clarified by centrifugation at 13,000 g for 30 min at 4 °C. Proteins were purified from the cell-free extract by nickel-nitrilotriacetic acid (Ni-NTA) affinity chromatography (Agarose Bead Technologies). The GEM-GECO1 protein was concentrated and the buffer of purified protein was exchanged to 10 mM 3-(N-morpholino)propanesulfonic acid (MOPS), 100 mM KCl, pH 7.2, supplemented with either 10 mM EGTA (Ca^{2+}-free sample) or 10 mM CaEGTA (Ca^{2+}-bound sample), using Amicon Ultra-4 Centrifugal Filter Unit (EMD Millipore Corporation). Absorption spectra of diluted samples were recorded on a DU-800 UV/visible spectrophotometer (Beckman) to ensure the absorbance of 392 nm (for Ca^{2+}-bound sample) or 398 nm (for Ca^{2+}-free sample) was above 2/mm for both undiluted samples.

GEM-GECO1 Site-Specific Mutagenesis. Synthetic DNA oligonucleotides used for GEM-GECO1 single mutagenesis experiments were purchased from Integrated DNA Technologies. The sequences of all oligonucleotides are provided in Table S4. QuikChange Lightning Single kit (Agilent Technologies) was used for site-directed single mutagenesis of GEM-GECO1 in pTorPE vector according to the manufacturer's instruction. Electrocompetent *E. coli* strain DH10B cells were transformed with the QuikChange product and cultured overnight at 37 °C on 10-cm Petri dishes of LB-agar supplemented with 200 μg/mL ampicillin and 0.0020% (wt/vol) L-arabinose.

Clones were picked and cultured in liquid LB medium supplemented with 200 μg/mL ampicillin and 0.0020% (wt/vol) L-arabinose at 37 °C overnight. Cells were harvested by centrifugation at 13,000 g for 2 min at 4 °C. Surfactant B-PER (Pierce) was used to lyse cells. After centrifugation at 13,000 g for 5 min at 4 °C, the cytoplasmic proteins including GEM-GECO1 and mutants in the supernatant were collected and purified by Ni-NTA affinity chromatography. The cell debris was treated for small-scale isolation of plasmid DNA using GeneJET miniprep kit (Fermentas); 5 μL of each purified sample was added into 50 μL of solution containing 10 mM MOPS, 100 mM KCl, pH 7.2 with either 10 mM EGTA (Ca^{2+}-free sample) or 10 mM CaEGTA (Ca^{2+}-bound sample) in a microplate well. Fluorescence spectra of GEM-GECO1 and its mutants in the presence and absence of Ca^{2+} were recorded on a Safire2 platereader (Tecan) with three replicates for each protein preparation and at least two independent preparations for each mutant. For excitation spectra, the emission intensity was measured at 535 nm. To acquire emission spectrum of each variant, excitation at 395 nm was used. The cDNA sequences for all GEM-GECO1 mutants were confirmed by dye terminator cycle sequencing using the BigDye Terminator Cycle Sequencing kit (Applied Biosystems).

Femtosecond Stimulated Raman Spectroscopy Measurements. The excited-state femtosecond stimulated Raman spectroscopy (FSRS) experimental setup was previously reported (2, 3). In brief, we use a femtosecond mode-locked Ti:sapphire oscillator (Mantis-5) and regenerative laser amplifier (Legend Elite; Coherent) to provide ∼35 fs, 2 mJ pulse centered at ∼800 nm with 1-kHz repetition rate. The output laser is split into three beams to generate a Raman pump–probe pair and an actinic pulse for photoexcitation. About 500-μW 400-nm actinic pulse is generated through frequency doubling a small portion of the fundamental pulse in a 0.3-mm-thick β-barium borate (BBO) crystal (type I, phase-matching angle $\theta = 27.8°$), followed by prism (Suprasil-1; CVI Melles Griot) compression to ∼40 fs. About 1.2 W of the laser output is dispersed by a gold reflective grating (1,200 grooves/mm, first-order wavelength at 750 nm, blaze angle of 26.7°) and passed through a 90-μm-wide slit to generate the Raman pump with 800-nm center wavelength, ∼6-mW power, and 3.5-ps pulse duration. The 100-nJ/pulse Raman probe beam at 840–960 nm (corresponding to ca. 600–2,000 cm^{-1} Stokes Raman shift to the 800-nm pump pulse) from supercontinuum white light is generated in a 2-mm thick Z-cut sapphire crystal and compressed with a fused silica prism pair to ∼35 fs, followed by a long-pass filter (RG830; Newport). The crossing angle between the Raman probe and actinic pulse or Raman pump is ∼3.5° with the probe situated between the other two pulses.

For exited-state FSRS, the Raman pump and probe pulses remain temporally fixed at time zero, and the preceding actinic pump is controlled by a stepper-motor-driven translation stage. The protein sample solution (OD ∼ 1/mm at 400 nm) is continuously flowed through a 1-mm pathlength quartz cell to avoid thermal effects and provides reasonable interaction length for the ensemble spectroscopic measurement (4). The stimulated Raman signal is collinear with the transmitted probe beam, which is selected to enter the spectrograph and dispersed by a 1,000-nm blaze, 600-grooves/mm grating, before being imaged onto a 1,340 × 100 CCD array (PIXIS 100F; Princeton Instruments). This ensures the fluorescence rejection capability of the FSRS setup (4, 5). We collect at least 12 sets of excited-state FSRS data with 3,000 shots per point, so the spectrum at each time delay (from –5 to 650 ps with various time steps, randomized in sequence to eliminate thermal effect or backslash, also limited by the length of the 10-cm translation stage that corresponds to ∼667 ps) is averaged for ≥18,000 times. The ground-state (GS) spectrum of the protein sample is collected periodically throughout the experiment to monitor sample conditions and provide a highly averaged trace for GS subtraction, and the retrieval of pure excited-state (ES) vibrational features after broad spectral baseline removal (6).

For kinetic analysis, individual Raman mode is least-squares fitted by a Gaussian curve with the center frequency and integrated intensity plotted against delay time. At least three time-resolved FSRS data sets were independently collected on different days to ensure reproducibility. The error bars in the ES vibrational peak kinetic plots (Figs. 3 and 4 and Figs. S2 and S3)

thus represent the "+/− σ" given that the average value has been taken for each data point at each time delay (the sample size is 3 so $n = 3$), and the spread is derived from the square root of the variance. Notably at each time delay, the FSRS experimental data average at least 18,000 excited-state Raman spectra so the signal-to-noise ratio is significantly enhanced over conventional continuous-wave (cw) Raman, and the spectral features can be clearly obtained. The multiexponential fit to the temporal profile of spectral features is all convoluted with the ∼140-fs full-width-at-half-maximum (FWHM) instrument response function, measured from the cross-correlation time between the femtosecond photoexcitation pulse and the Raman probe pulse.

More Insights into Excited-State Vibrational Peak Dynamics from FSRS. Quantitative analysis of the ES peak frequency and intensity changes will lead to a clear portrait of atomic motions on the femtosecond to picosecond timescale following photoexcitation. Notably, the 1,663 and 1,004 cm^{-1} modes (Fig. S1) are likely protein backbone modes because they do not appear in the ES spectrum after GS subtraction, and they are also absent in the Raman spectrum of a model compound for the GFP chromophore (7–9). The 1,138/1,147 cm^{-1} phenol H-rocking mode in photoexcited Ca^{2+}-free/bound proteins exhibits the first decay time constant greater than 1 ps (i.e., 1.3/1.6 ps, respectively; Table S1), corroborating its assignment to a localized phenol H-rocking mode associated with a neutral chromophore, hence the longer initial decay to reach the vibrationally relaxed A* state. In contrast, the neighboring higher-frequency mode at 1,180 cm^{-1} exhibits a much faster initial decay time constant of 630–730 fs, which agrees with its assignment of a more delocalized mode associated with a partially deprotonated chromophore. Following photoexcitation, the 1,180 cm^{-1} mode thus relaxes faster as the chromophore undergoes conformational motions out of the Franck–Condon (FC) region. The second (much longer) decay time constant reports on the dominant ES structural evolution on the picosecond timescale, which directly reports on whether or not excited-state proton transfer (ESPT) from A* to an effectively deprotonated I* state is the dominant reaction pathway.

The blueshift of the chromophore phenolic C—O stretching mode at 1,247/1,250 to 1,265 cm^{-1} is observed in Ca^{2+}-free/bound GEM-GECO1 following 400-nm excitation (Fig. S1). This is because photoexcitation shifts electrons from the hydroxyl end toward the phenolic ring starting at time zero, hence strengthening the C—O bond to some extent. This initial step of electronic redistribution going from A→A* is conserved for the chromophore due to its photoacidity, regardless of its ESPT capabilities. The similarity of the mode dynamics on the sub-picosecond timescale attests the point, whereas the subsequent picosecond dynamics manifest the dramatic effect of ESPT without Ca^{2+} vs. trapped A* state with Ca^{2+}. Moreover, the first decay time constant of the 1,305 cm^{-1} mode (540 fs) is in general faster than other high-frequency modes in the Ca^{2+}-free protein (Table S1), suggesting that this bridge-H rocking mode projects strongly onto the initial wavepacket trajectory out of the FC region for the chromophore in preparation for ESPT.

As ESPT progresses, the 1,570 cm^{-1} mode redshifts by ∼30 cm^{-1} in the Ca^{2+}-free protein that reflects the electron conjugation change on the imidazolinone ring and possible contribution from the quinonelike character of the phenol ring in the intermediate green fluorescent state I*. In resonance and surface-enhanced Raman experiments, this mode is the most prominent and has been implicated as the strongest mode along the initial reaction coordinate (8); lack of probe photons on the red side of the current spectral window in our setup accounts for a weakened peak with reduced signal-to-noise ratio. The absence of this mode redshift is apparent with Ca^{2+} (Fig. 2*B*).

The modes at 967, 885, and 819 cm^{-1} (Fig. S2) are relatively long-lived in comparison with the modes above 1,000 cm^{-1}. These modes are more persistent in the Ca^{2+}-bound protein, whereas the 967 cm^{-1} mode blueshifts by ∼10 cm^{-1} after ∼30 ps in the Ca^{2+}-free protein that suggests I* formation. This trend is consistent with time-dependent density functional theory (TD-DFT) calculations (10) that predict a blueshift of this mode from GS to ES and the formation of I* following ESPT (Fig. 2*A*). The imidazolinone ring deformation mode at 885 cm^{-1} shows an overall larger decay time constant than the phenol ring modes at 819 and 967 cm^{-1} (Table S1) in both the Ca^{2+}-free and -bound proteins, consistent with the argument that the ES structural evolution of the chromophore starts from the phenol ring (11) and propagates toward the imidazolinone ring, which takes relatively longer time to react and relax.

Structural Insights for the Ca^{2+}-Free GEM-GECO1 from Molecular Dynamics Simulations. To correlate the key mutations with functional changes of the local environment of the chromophore, we performed the equilibrium molecular dynamics (MD) simulations using Amber12 program (12). The coordinates of the Ca^{2+}-free GCaMP2 (PDB ID 3EKJ) (13) were used as the starting point. Because of its deficient structure, the missing part of CaM was padded with an independent Ca^{2+}-free CaM crystal structure (PDB ID 1CFD) (14) and the M13 helix was added from the Ca^{2+}-bound GCaMP3 (PDB ID 3SG3) (15). The crystallized water molecules from all three structures were kept. All of the GEM-GECO1 point mutations (1) were made using SwissPDB Viewer (16) and the missing residues (e.g., residue number 144–157 in the loop region) were added. Hydrogen (H) atoms for the protein were then added using the AmberTools13 package. Afterward, these structures were neutralized and solvated with 66,791 TIP3P water molecules within 20-Å radius of the protein. The entire protein complex system went through 5,000 steps of energy minimization, followed by 60-ps gradual heating from 0 to 300 K using the Langevin thermostat with a collision frequency of 2 ps^{-1}, and 100 ps further equilibration without restraints. Subsequently, a 10-ns MD simulation was performed under constant temperature at 300 K, with a time step of 2 fs. The SHAKE method (an Amber algorithm based on dynamics to perform bond-length constraints) was used to keep all bonds involving the H atoms rigid. The output coordinates were recorded every 2 ps.

From the 10-ns trajectory, the potential energy of the system as a function of time was plotted and we selected the conformational snapshot with the lowest potential energy to represent the Ca^{2+}-free GEM-GECO1 structure (Fig. S4). During this MD simulation, the chromophore rigidity was not maintained very well, indicative of its flexibility in the protein pocket. The structures of CaM and M13 domains showed significant differences from the Ca^{2+}-bound GCaMP proteins [e.g., PDB ID 3EVR (17), 3SG3]. The CaM unit does not wrap around M13 and it remains extended as two subdomains, which conforms to the Ca^{2+}-free environment. In comparison with the starting structural coordinates, the orientation of M13 unit rotates upward due to the added CaM unit, which makes the β-barrel opening larger (Fig. S4*A*). In the lowest-energy structure, the chromophore phenol ring is slightly out of plane with the imidazolinone ring. In comparison with 3EKJ, the phenolic hydroxyl group of the chromophore occupies an almost conserved location, but the hydroxyl group of S118 rotates to a lower position, which makes its oxygen atom more in plane with the chromophore phenol ring. Notably, after the aforementioned energy minimization, two water molecules exist between the chromophore phenolic hydroxyl group and S118. One of the water molecules is largely in plane with the chromophore phenol ring and forming H bonds with S118 and the chromophore (Fig. S4*B*). Following the initial structural motion of the chromophore in the electronic excited

state, the involvement of adjacent E135 in the ESPT chain can be readily facilitated by its sidechain motion to be in a H-bonding geometry to S118 (Fig. 5). In the absence of a crystal structure for GEM-GECO1, the MD simulation yields a useful geometry for the Ca^{2+}-free protein with integrated CaM and M13 units and all of the necessary GEM-GECO1-specific mutations. It also provides detailed structural information particularly pertaining to the local environment of the chromophore to the interpretation of the conformational dynamics data from our FSRS measurements.

Functional Role of a Dominant Skeletal Motion along the ESPT Multidimensional Reaction Coordinate. Our experimental data strongly argue that the observed phenolate vibrational motion plays a functional role in modulating ESPT, which represents a transferrable concept from our previous report on wild-type (wt) GFP that identified a different dominant vibrational motion (4). It is notable that the local environment of the chromophore determines its potential energy surface (PES), which includes the p*K*a of the chromophore in S_0 and S_1, the dominant low-frequency mode that projects strongly onto the initial reaction coordinate (typically on the femtosecond to picosecond timescale), and the ESPT rate on the picosecond timescale after the initial crucial proton motions (photochemical events). We hereby summarize our findings in a logical way to further corroborate this important conclusion regarding the functional role of the 170 cm^{-1} mode in the Ca^{2+}-free GEM-GECO1 biosensor:

i) The ∼170 cm^{-1} mode is an in-plane phenol ring rocking motion that brings the phenolic proton closer and farther away from a nearby Ser118 residue via a bridging H_2O molecule. Because the crystal structure of the Ca^{2+}-free GEM-GECO1 is unavailable, we perform a 10-ns MD simulation and find the conformational snapshot with the lowest potential energy (Fig. S4). The nuclear coordinate change of the 170 cm^{-1} mode is highly relevant to modulate the H-bonding geometry in the immediate vicinity of the chromophore phenolic end, particularly in a local environment where Ser118 along the ESPT chain is largely in plane with the phenolic hydroxyl group.

ii) The ∼170 cm^{-1} mode coherently modulates the high-frequency modes following photoexcitation, as a result, we observe clear spectral oscillations (i.e., quantum beats). The mere existence of a number of low-frequency modes that strongly couple to the electronic degree of freedom cannot manifest a prominent single-frequency oscillation, on the contrary, the projection onto the ESPT reaction coordinate matters. In wtGFP, the local environment involves a conserved H_2O molecule above and to one side of the phenolic hydroxyl group, and Thr203 and His148 residues on opposite sides of the phenolic ring plane: a ∼120 cm^{-1} wagging mode thus becomes the dominant motion to facilitate the initial phase of ESPT as the rest of the ESPT chain optimizes on the longer picosecond timescale. In the Ca^{2+}-free GEM-GECO1, the local environment changes and now involves labile H_2O molecules due to the β-barrel opening as well as an in-plane Ser118 residue nearby, therefore a ∼170 cm^{-1} skeletal rocking mode becomes the dominant motion to modulate the H-bonding network in the vicinity of the chromophore phenolic end. It is required to play the functional role of setting up the stage for ESPT because the starting S_0 geometry of the H-bonding network is not optimized for efficient proton transfer in S_1 (2–4, 18–21). That is also why we observe the appearance of the I* modes (e.g., 1,305 cm^{-1} mode after ∼3 ps; Figs. 2*A* and 3*B*) after the A* mode oscillations (e.g., 1,265 and 1,570 cm^{-1} modes before ∼2 ps; Fig. 4), strongly indicative of causality.

iii) In typical intensiometric GCaMP proteins, the Ca^{2+}-free protein has weaker fluorescence than the Ca^{2+}-bound protein. The fact that neither the absorption nor fluorescence properties of the P377R mutant of GEM-GECO1 change in the presence of Ca^{2+} (Figs. S5*F* and S6) actually suggests that some functional motions occur within the different conformational space sensed by the chromophore surrounded by protein pocket residues and labile H_2O molecules. Future work is needed to specifically dissect the initial reaction coordinate leading to the ESPT reaction barrier, ideally with the Ca^{2+}-free/bound P377R GEM-GECO1 mutant samples, but it is conceivable from aforementioned data and reasoning that a particular low-frequency skeletal mode could be the dominant motion without Ca^{2+}, which effectively gates the initial structural evolution on the multidimensional potential energy surface of the photoexcited chromophore. Otherwise, the Ca^{2+}-free protein is expected to be less efficient to emit green fluorescence when excited at ∼400 nm, which is not what we observed in the experiment (Figs. S5*F* and S6).

In essence, the quantum beats observed in this work (Fig. 4 and Fig. S2) reveal the anharmonic modulation (4, 19–23) of the high-frequency vibrational modes by a dominant low-frequency skeletal motion in the Ca^{2+}-free GEM-GECO1, which shows prominent activity on the subpicosecond to picosecond timescale before ESPT. This ∼170 cm^{-1} mode is essentially determined by the protein environment that hosts the embedded chromophore, and the vibrational motion is functional because it projects strongly onto the initial ESPT reaction coordinate that is multidimensional in nature. In contrast, this mode diminishes in the Ca^{2+}-bound GEM-GECO1 while other low-frequency modes compete for energy dissipation (Fig. S3, *Inset*), leading to A* trapping and ESPT inhibition (there might still be some ESPT capability of the chromophore facilitated by the 170 cm^{-1} mode as evinced by the 508-nm emission shoulder in Fig. 1*B*). The thermodynamic properties of the relative p*K*a of the chromophore phenolate and the associated water molecules are part of the local environment parameters, which affect the PES but not ESPT directly. The causative connection between the uncovered skeletal motion and the subsequent ESPT is thus established. It is evident from all of the aforementioned discussions that one unique advantage of using FSRS to study photosensitive biomolecules is to uncover one fraction, albeit an extremely significant fraction in the initial reaction stage, of the multidimensional excited-state PES (4).

Additional Results and Discussion on Site-Directed Mutagenesis of GEM-GECO1. We observed a relatively uniform response of A* to I* emission ratio in the Ca^{2+}-free protein mutants upon 395 nm excitation in Figs. S5 and S6*A* (except S118G to be discussed later), and noticeable decrease of that emission ratio existed for all of the mutants in the Ca^{2+}-bound state (P377R essentially abolishes the dual-emission ability) in comparison with GEM-GECO1. As a result, these residues all represent functional sites around the chromophore that either play a dominant or auxiliary role in affecting the ground-state and excited-state properties of the fluorescent protein, which lead to the unique dual-emission imaging ability of GEM-GECO1. Detailed analysis of the absorption and emission spectra of all of the purified protein mutants that we made can be found below.

Proteins with either P60L or E61H in the M13 to FP linker exhibited Ca^{2+} responses that were noticeably different from those of GEM-GECO1 itself, suggesting that either residue may play a functional role in the overall modulation of fluorescence properties (Fig. S5 *B* and *C*). In particular, a significant increase in B state (anionic GS) population with the E61H variant in the absence of Ca^{2+}, relative to GEM-GECO1, suggests that E61 partially contributes to the stabilization of the neutral form of

the GS chromophore (Figs. S5*C*, *Inset*, and S6), likely due to the conformation of the ionizable sidechain of E61. Notably, E61H also shows a shift of equilibrium population from A* to I* upon Ca^{2+} binding (Figs. S5*C* and S6*A*), indicating that E61 hinders ESPT in the Ca^{2+}-bound state. Regarding the P60L mutant, an even larger decrease in the A* to I* emission ratio (excitation at 395 nm) for the Ca^{2+}-bound protein was observed (Figs. S5*B* and S6*A*), and the fluorescence of the deprotonated chromophore (B state) increases about twofold upon binding to Ca^{2+} (Figs. S5*B* and S6*C*). This indicates that P60 does contribute to ESPT disruption upon Ca^{2+} binding so P60L greatly reduces the dual-emission color contrast from green to blue emission. Given the slight effect of the E61H mutation, we suggest that the P60L mutation may influence the fluorescent properties via a conformational change of N62 or V63, both of which are in closer proximity to the chromophore phenolic end.

Proteins with V116T or S118G mutations in the FP domain exhibit fluorescence spectra and Ca^{2+}-dependent responses that are similar to those of GEM-GECO1, with a few notable differences. V116T and S118G both exhibit poor protein-folding efficiency at 37 °C so structural variation particularly at the local environment level is possible. In comparison with GEM-GECO1, S118G mutant shows a substantial increase in the A* to I* emission ratio for the Ca^{2+}-free protein (Figs. S5*E*, *Inset*, and S6*A*) with S118G exhibiting a twofold higher ratio. This result suggests that S118 has a role besides structured water molecules in facilitating ESPT (A*→I*) in the Ca^{2+}-free state of GEM-GECO1. Both variants also have a substantial increase in the 474 to 402 nm excitation ratio (Fig. S6*B*) and decrease in the green emission upon 395-nm excitation (Fig. S6*D*), indicative of reduced quantum yield of I* green fluorescence regardless of the presence or absence of Ca^{2+}. Residue V116 is situated below the chromophore ring plane and its inability to participate in a H-bonding network with the chromophore (24, 25) may be playing a role in the 170 cm^{-1} in-plane phenol ring rocking motion to facilitate ESPT in the Ca^{2+}-free protein (see main text and Fig. 5).

The P377R variant has the largest decrease of A* to I* emission ratio in the presence of Ca^{2+} (Fig. S6*A*), indicating that this protein cannot effectively disrupt ESPT to thereby fluoresce from a trapped A* state. This result indicates that P377 plays a critical role in preventing ESPT in the presence of Ca^{2+}. Because P377 is not itself ionizable and most likely does not interact directly with the chromophore, it is plausible that this residue is exerting influence through conformational positioning of other nearby, yet unidentified, residues at the FP–CaM interface. Because the formation of the interfacial region at the Ca^{2+}-bound state reduces access of water molecules to the chromophore, a hydrophobic residue X (potential candidates include M375 and M379 near P377) of CaM can point to the phenol group of the chromophore and exclude nearby water molecules, which lead to trapping of the A* state upon UV light excitation and blueshift of the absorption peak (Fig. 1*B*; 398 → 392 nm for the Ca^{2+}-free → Ca^{2+}-bound protein). Because the ground-state Raman spectrum of GEM-GECO1 remains largely unchanged upon Ca^{2+} binding (Fig. S1*C*), we consider that the blueshift of the absorption maximum is mainly due to the modification of the excited-state PES by those nearby hydrophobic residues (26). In the P377R mutant, this blueshift disappears (Fig. S5*F*), confirming that P377 is crucial to establish the hydrophobic local environment to inhibit ESPT. Meanwhile, the aforementioned P60 may play a minor role in fine tuning the geometry of residue X by adjusting the position and orientation of the M13/CaM complex. That explains the second-largest drop of the A* over I* emission in the Ca^{2+}-bound protein of the P60L mutant (Figs. S5*B* and S6*A*).

Further Discussion of Fluorescence Modulation Mechanism in GEM-GECO1. Time-resolved FSRS spectra stem from the conformational dynamics of the chromophore surrounded by the protein pocket. Because only the chromophore absorbs at 400 nm, the rest of the protein acts as a transparent medium and thus does not contribute to the ES spectrum after GS subtraction (4, 6). It was shown that the fluorescence of canonical GCaMPs is primarily modulated by Ca^{2+}-dependent changes in chromophore pK_a and solvent access to the chromophore (13, 17). In comparison with wtGFP, the GCaMP chromophore is more solvent accessible due to circular permutation of the β-barrel (Fig. 1*A*). GCaMP3, for example, lacks a true equivalent of H148 that plays a key functional role in wtGFP (Table S3). However, an interfacial R377 of CaM is considered to be functionally similar even though it is much farther away and the interaction with the chromophore is likely mediated by structured water molecules (13, 17).

In the Ca^{2+}-free GEM-GECO1, the tertiary-structure-altering L60P mutation from its GCaMP progenitor may extend the β-strand at the C terminus hence excluding more solvent and pushing away E61, therefore favoring ESPT. This is consistent with our mutagenesis studies that show the Ca^{2+}-free protein with E61H mutation having more deprotonated chromophore in GS (Figs. S5*C*, *Inset*, and S6*C*) because H61 is a better proton acceptor to coordinate the phenolic end of the chromophore, functionally similar to H148 in wtGFP that also promotes a small population of the partially deprotonated chromophore in GS (27). Also in GEM-GECO1, the labile (not conserved) water molecules in the partially open β-barrel pocket and the presence of the T116V mutation at the equivalent wtGFP position of T203 (Table S3) contribute to the ESPT efficiency decrease and the lower quantum yield (QY) (~0.31, for 511-nm emission in the Ca^{2+}-free protein; ref. 1) in comparison with wtGFP (QY ~ 0.8 for 508-nm emission; ref. 28) upon ~400 nm excitation.

In particular, the T116V mutation in GCaMPs mildly affects their fluorescence behavior (13, 29) but promotes a neutral GS chromophore. Fig. 1*B* shows this effect in GEM-GECO1 that has a valine residue (V116) at the corresponding position below the chromophore ring plane. Upon V116T mutagenesis reversion into GEM-GECO1, a slight increase of the anionic GS chromophore population (Fig. S6 *B* and *C*) as well as decreased I* emission (via ESPT process from A*; Fig. S6*D*) in the Ca^{2+}-free protein were observed. This result suggests the functional role of a largely in-plane vibrational motion that facilitates the ESPT reaction in the Ca^{2+}-free GEM-GECO1.

The observed 170 cm^{-1} phenol-ring in-plane rocking motion may be ubiquitous in GFP-like proteins that lack the strategic threonine residue (e.g., T203 in wtGFP, with the sidechain hydroxyl for H bonding) but are still capable of ESPT. The reaction speed depends on the distance from the chromophore phenolic end to the serine residue along the ESPT path, the time for bridging water molecule(s) to rearrange, and the degree of I* stabilization by surrounding residues. In comparison with the previously reported 120 cm^{-1} phenol-ring out-of-plane wagging motion that gates ESPT (4), it is evident that ESPT typically requires one dominant low-frequency skeletal motion to facilitate directional proton transfer, and the characteristic skeletal motion will be selected on the basis of the chromophore local environment. The PES dictates the wavepacket Hamiltonian thus strongly projects certain structurally relevant modes along the chemical reaction coordinate, and in this excited-state case, bioluminescence.

Full authorship of Gaussian 09

Gaussian 09, Revision B.1, M. J. Frisch, G. W. Trucks, H. B. Schlegel, G. E. Scuseria, M. A. Robb, J. R. Cheeseman, G. Scalmani, V. Barone, B. Mennucci, G. A. Petersson, H. Nakatsuji, M. Caricato, X. Li, H. P. Hratchian, A. F. Izmaylov, J. Bloino, G. Zheng,

J. L. Sonnenberg, M. Hada, M. Ehara, K. Toyota, R. Fukuda, J. Hasegawa, M. Ishida, T. Nakajima, Y. Honda, O. Kitao, H. Nakai, T. Vreven, J. A. Montgomery, Jr., J. E. Peralta, F. Ogliaro, M. Bearpark, J. J. Heyd, E. Brothers, K. N. Kudin, V. N. Staroverov, R. Kobayashi, J. Normand, K. Raghavachari, A. Rendell, J. C. Burant, S. S. Iyengar, J. Tomasi, M. Cossi, N. Rega, J. M. Millam, M. Klene, J. E. Knox, J. B. Cross, V. Bakken, C. Adamo, J. Jaramillo, R. Gomperts, R. E. Stratmann, O. Yazyev, A. J. Austin, R. Cammi, C. Pomelli, J. W. Ochterski, R. L. Martin, K. Morokuma, V. G. Zakrzewski, G. A. Voth, P. Salvador, J. J. Dannenberg, S. Dapprich, A. D. Daniels, Ö. Farkas, J. B. Foresman, J. V. Ortiz, J. Cioslowski, and D. J. Fox, Gaussian, Inc., Wallingford CT, 2009.

1. Zhao Y, et al. (2011) An expanded palette of genetically encoded Ca^{2+} indicators. *Science* 333(6051):1888–1891.
2. Liu W, Han F, Smith C, Fang C (2012) Ultrafast conformational dynamics of pyranine during excited state proton transfer in aqueous solution revealed by femtosecond stimulated Raman spectroscopy. *J Phys Chem B* 116(35):10535–10550.
3. Han F, Liu W, Fang C (2013) Excited-state proton transfer of photoexcited pyranine in water observed by femtosecond stimulated Raman spectroscopy. *Chem Phys* 422(0):204–219.
4. Fang C, Frontiera RR, Tran R, Mathies RA (2009) Mapping GFP structure evolution during proton transfer with femtosecond Raman spectroscopy. *Nature* 462(7270):200–204.
5. McCamant DW, Kukura P, Yoon S, Mathies RA (2004) Femtosecond broadband stimulated Raman spectroscopy: Apparatus and methods. *Rev Sci Instrum* 75(11):4971–4980.
6. Frontiera RR, Fang C, Dasgupta J, Mathies RA (2012) Probing structural evolution along multidimensional reaction coordinates with femtosecond stimulated Raman spectroscopy. *Phys Chem Chem Phys* 14(2):405–414.
7. Bell AF, He X, Wachter RM, Tonge PJ (2000) Probing the ground state structure of the green fluorescent protein chromophore using Raman spectroscopy. *Biochemistry* 39(15):4423–4431.
8. Schellenberg P, Johnson E, Esposito AP, Reid PJ, Parson WW (2001) Resonance Raman scattering by the green fluorescent protein and an analogue of its chromophore. *J Phys Chem B* 105(22):5316–5322.
9. He X, Bell AF, Tonge PJ (2002) Isotopic labeling and normal-mode analysis of a model green fluorescent protein chromophore. *J Phys Chem B* 106(23):6056–6066.
10. Frisch MJ, et al. (2009) *Gaussian 09, Revision B.1* (Gaussian, Inc., Wallingford, CT).
11. Granucci G, Hynes JT, Millie P, Tran-Thi T-H (2000) A theoretical investigation of excited-state acidity of phenol and cyanophenols. *J Am Chem Soc* 122(49):12243–12253.
12. Case DA, et al. (2012) AMBER 12. (University of California, San Francisco, CA).
13. Akerboom J, et al. (2009) Crystal structures of the GCaMP calcium sensor reveal the mechanism of fluorescence signal change and aid rational design. *J Biol Chem* 284(10):6455–6464.
14. Kuboniwa H, et al. (1995) Solution structure of calcium-free calmodulin. *Nat Struct Biol* 2(9):768–776.
15. Akerboom J, et al. (2012) Optimization of a GCaMP calcium indicator for neural activity imaging. *J Neurosci* 32(40):13819–13840.
16. Guex N, Peitsch MC (1997) SWISS-MODEL and the Swiss-PdbViewer: An environment for comparative protein modeling. *Electrophoresis* 18(15):2714–2723.
17. Wang Q, Shui B, Kotlikoff MI, Sondermann H (2008) Structural basis for calcium sensing by GCaMP2. *Structure* 16(12):1817–1827.
18. Lochbrunner S, Wurzer AJ, Riedle E (2000) Ultrafast excited-state proton transfer and subsequent coherent skeletal motion of 2-(2′-hydroxyphenyl)benzothiazole. *J Chem Phys* 112(24):10699–10702.
19. Lochbrunner S, Stock K, Riedle E (2004) Direct observation of the nuclear motion during ultrafast intramolecular proton transfer. *J Mol Struct* 700(1-3):13–18.
20. Huse N, et al. (2005) Anharmonic couplings underlying the ultrafast vibrational dynamics of hydrogen bonds in liquids. *Phys Rev Lett* 95(14):147402.
21. Kukura P, Frontiera R, Mathies RA (2006) Direct observation of anharmonic coupling in the time domain with femtosecond stimulated Raman scattering. *Phys Rev Lett* 96(23):238303.
22. Fang C, Senes A, Cristian L, DeGrado WF, Hochstrasser RM (2006) Amide vibrations are delocalized across the hydrophobic interface of a transmembrane helix dimer. *Proc Natl Acad Sci USA* 103(45):16740–16745.
23. Wilson KC, Lyons B, Mehlenbacher R, Sabatini R, McCamant DW (2009) Two-dimensional femtosecond stimulated Raman spectroscopy: Observation of cascading Raman signals in acetonitrile. *J Chem Phys* 131(21):214502–214515.
24. Kummer AD, et al. (2000) Effects of threonine 203 replacements on excited-state dynamics and fluorescence properties of the green fluorescent protein (GFP). *J Phys Chem B* 104(19):4791–4798.
25. Jung G, Wiehler J, Zumbusch A (2005) The photophysics of green fluorescent protein: Influence of the key amino acids at positions 65, 203, and 222. *Biophys J* 88(3):1932–1947.
26. Hanson GT, et al. (2002) Green fluorescent protein variants as ratiometric dual emission pH sensors. 1. Structural characterization and preliminary application. *Biochemistry* 41(52):15477–15488.
27. Shu X, et al. (2007) Ultrafast excited-state dynamics in the green fluorescent protein variant S65T/H148D. 1. Mutagenesis and structural studies. *Biochemistry* 46(43):12005–12013.
28. Chattoraj M, King BA, Bublitz GU, Boxer SG (1996) Ultra-fast excited state dynamics in green fluorescent protein: Multiple states and proton transfer. *Proc Natl Acad Sci USA* 93(16):8362–8367.
29. Chen Y, et al. (2013) Structural insight into enhanced calcium indicator GCaMP3 and GCaMPJ to promote further improvement. *Protein Cell* 4(4):299–309.

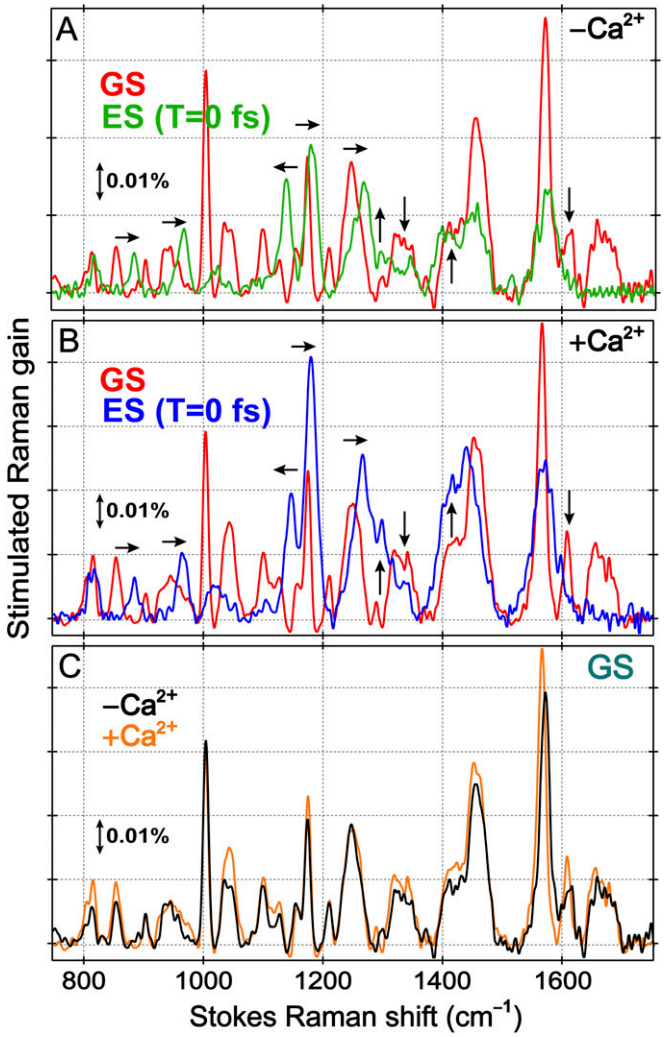

Fig. S1. Raman spectral comparison of GEM-GECO1 in S_0 and S_1 at photoexcitation time zero. (*A*) GS (red) and $T = 0$ fs ES (green) Raman spectra of the Ca^{2+}-free protein. (*B*) GS (red) and $T = 0$ fs ES (blue) Raman spectra of the Ca^{2+}-bound protein. (*C*) Ground-state Raman spectra of the Ca^{2+}-free (black) and bound (orange) proteins. Besides the broadband Raman probe pulse, the GS spectra were recorded with a ∼800 nm Raman pump, and an additional ∼400 nm actinic pump was used to collect the ES spectra. Because only ∼10% of the GS population converts to ES via photoexcitation, resonance enhancement is achieved in S_1 that leads to comparable spectral intensities with those in S_0 (4). Both protein samples had an optical absorbance of ∼1/mm at 400 nm. The absolute stimulated Raman gain strength of 0.01% is shown with the double-arrowed line. The similarity between the GS spectra in *C* regardless of Ca^{2+} binding (Table S1) reveals the largely conserved nature of the protein pocket in S_0 at thermal equilibrium. The time-resolved spectral differences (Figs. 2 and 3) are more significant than the static ground-state differences not only owing to resonance enhancement in S_1, but also due to the altered structural evolution pathways of GEM-GECO1 in the excited state upon Ca^{2+} binding. The main frequency shifts and intensity changes of the chromophore modes upon photoexcitation are indicated by black arrows in *A* and *B*, which are largely induced by ultrafast (i.e., <140 fs the instrument cross-correlation time) electronic redistribution within the FC region.

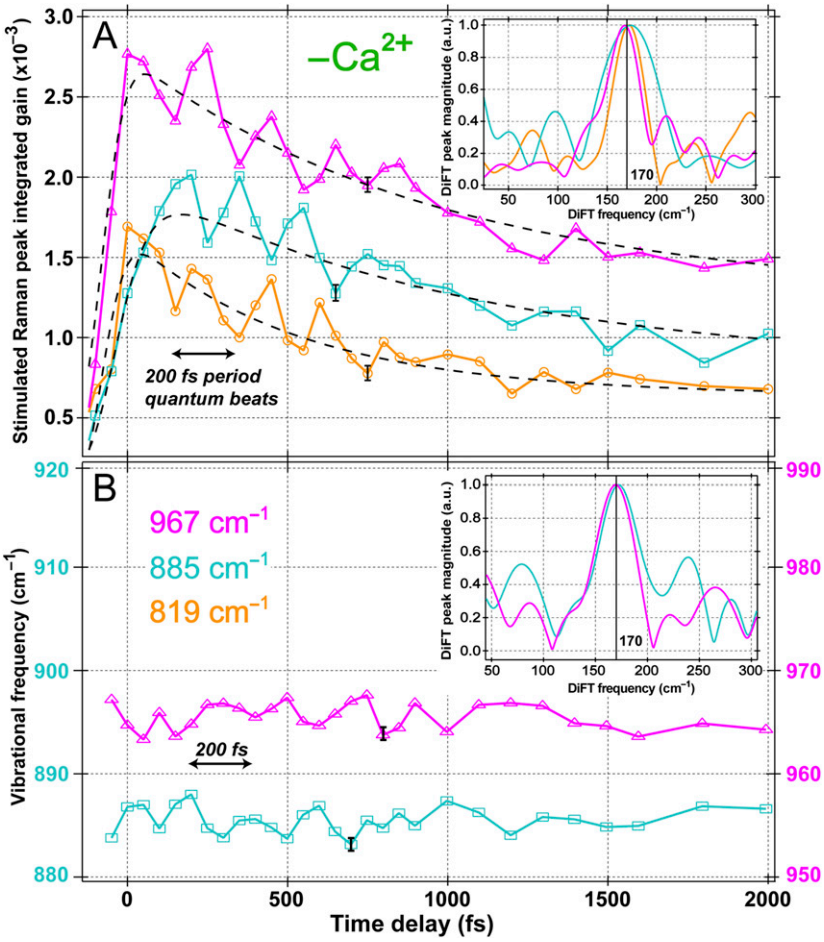

Fig. S2. Temporal evolution and quantum beats of three vibrational modes between 800 and 1,000 cm^{-1} of the Ca^{2+}-free GEM-GECO1 following 400-nm photoexcitation. (*A*) Peak intensity oscillations of the three stimulated Raman modes within 2 ps. The two phenol ring deformation modes at 819 and 967 cm^{-1} clearly oscillate in phase, whereas the 885 cm^{-1} mode oscillation is out of phase. This is attributed to a periodically modulated electronic distribution over the chromophore two-ring system due to the impulsively excited coherent motion at ∼170 cm^{-1} (Figs. 4 and 5), shown in the *Inset*, which modifies the geometry of the phenol ring and its surroundings to facilitate subsequent ESPT with a ∼30 ps time constant (Table S1). These modes have been offset vertically to manifest the coherent oscillatory features. The underlying modulation mode at ∼170 cm^{-1} (marked by the vertical black line in the *Inset*) is retrieved after performing the discrete Fourier transform (DiFT) of the quantum beats, which are oscillatory residuals after subtracting the data traces with the multi-exponential fits (black dashed lines) within 2 ps. (*B*) The frequencies of the 967 and 885 cm^{-1} modes also manifest 180° out-of-phase oscillations relative to each other with a ∼200 fs modulation period (shown by double-arrowed lines). The initial frequency redshift of the 967 cm^{-1} phenol deformation mode (magenta, right axis) and concomitant rise of the 885 cm^{-1} imidazolinone mode (cyan, left axis) is consistent with the initial electronic redistribution across the conjugated ring system of the chromophore following photoexcitation. The typical error bar (SD) for each experimental trace is depicted on one data point in the middle region. The DiFT spectra of the frequency quantum beats are shown in the *Inset*, also manifesting a dominant low-frequency mode at ∼170 cm^{-1} and the anharmonic coupling between this collective skeletal motion and the other high-frequency vibrational modes along the ESPT reaction coordinate.

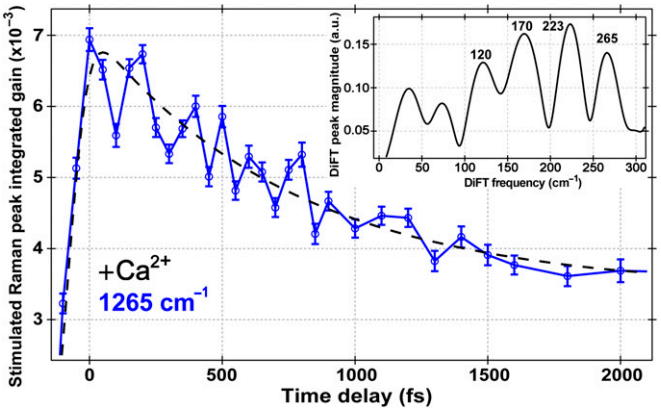

Fig. S3. Temporal evolution and intensity oscillation of the 1,265 cm^{-1} excited-state marker band of the Ca^{2+}-bound GEM-GECO1 following 400-nm photoexcitation. The oscillatory pattern has no well-defined period and the discrete Fourier transform yields multiple underlying modulation modes below 300 cm^{-1} (*Inset*) that is different from one dominant ~170 cm^{-1} mode in the Ca^{2+}-free protein (Figs. 4 and 5). The data trace is in blue whereas the incoherent exponential fit convoluted with the ~140 fs instrument response function is shown as the black dashed line. Error bars represent the SD of the Gaussian-fitted peak area (n = 3). The 120 cm^{-1} mode is likely associated with a previously observed phenoxyl ring wagging motion of the chromophore that gates ESPT in wtGFP (4). The varied functional roles played by these low-frequency modes in different local environments are discussed in the main text.

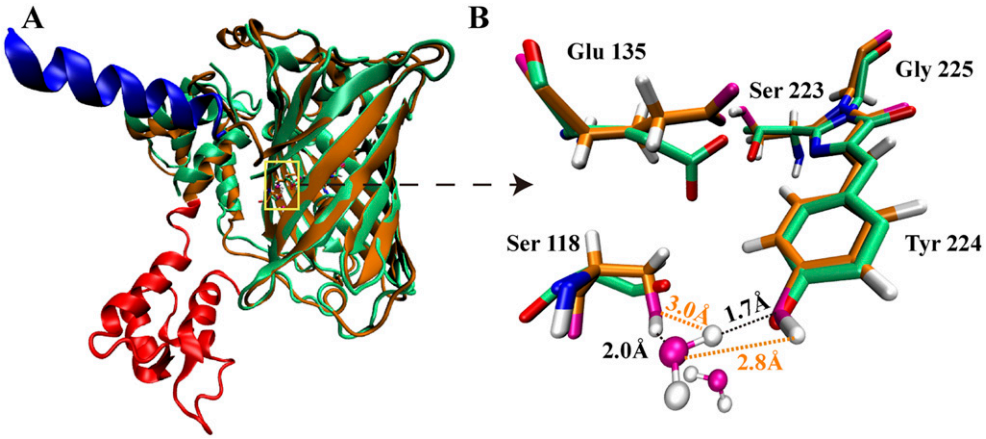

Fig. S4. Representative structure of GEM-GECO1 in the Ca^{2+}-free state from molecular dynamics simulations. (*A*) Overlay of the Ca^{2+}-free GCaMP2 crystal structure (PDB ID 3EKJ, shown in green) and the lowest-potential-energy ground-state structure of the Ca^{2+}-free GEM-GECO1 protein from MD simulations (shown in orange), wherein the patched M13 helix is shown in blue, and the added CaM part in red. The chromophore location near the β-barrel opening is indicated by the yellow box. (*B*) Enlarged chromophore pocket structure from 3EKJ (green, oxygen atoms depicted in red) and the lowest-energy structure from MD simulation (orange, oxygen atoms depicted in magenta). The black or orange dashed lines represent the H bonds in the vicinity of the phenolic hydroxyl group of the chromophore, potentially involving S118 and a bridging water molecule that could adopt multiple orientations in a protein environment (especially with the β-barrel opening). The E135 sidechain forms H bonds with surrounding water molecules in this ground-state equilibrium structure, but the sidechain flexibility may make E135 relevant for H-bonding in S_1 and particularly for ESPT (4, 28) in the Ca^{2+}-free protein. Nitrogen and hydrogen atoms are shown in blue and white, respectively.

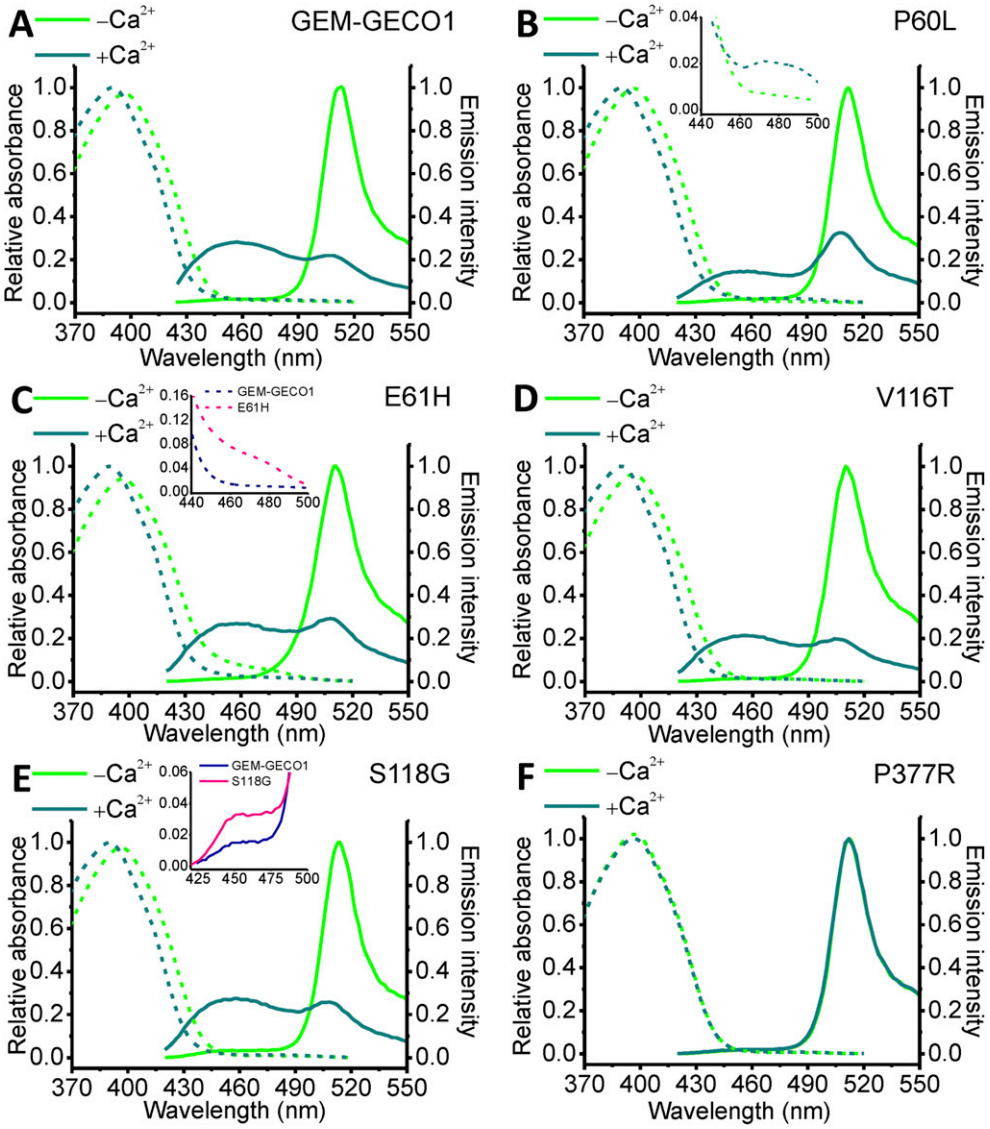

Fig. S5. Absorption and emission spectra of GEM-GECO1 and its single-residue mutants. (*A*) GEM-GECO1. (*B*) P60L, the *Inset* shows the enlarged normalized absorption spectra from 440 to 500 nm. (*C*) E61H, the *Inset* shows the comparison between the normalized absorption spectra of GEM-GECO1 and the E61H variant without Ca^{2+}; (*D*) V116T; (*E*) S118G, the *Inset* shows the comparison between the normalized emission spectra of GEM-GECO1 and the S118G variant without Ca^{2+}. (*F*) P377R, showing no dual-emission capability for Ca^{2+} sensing.

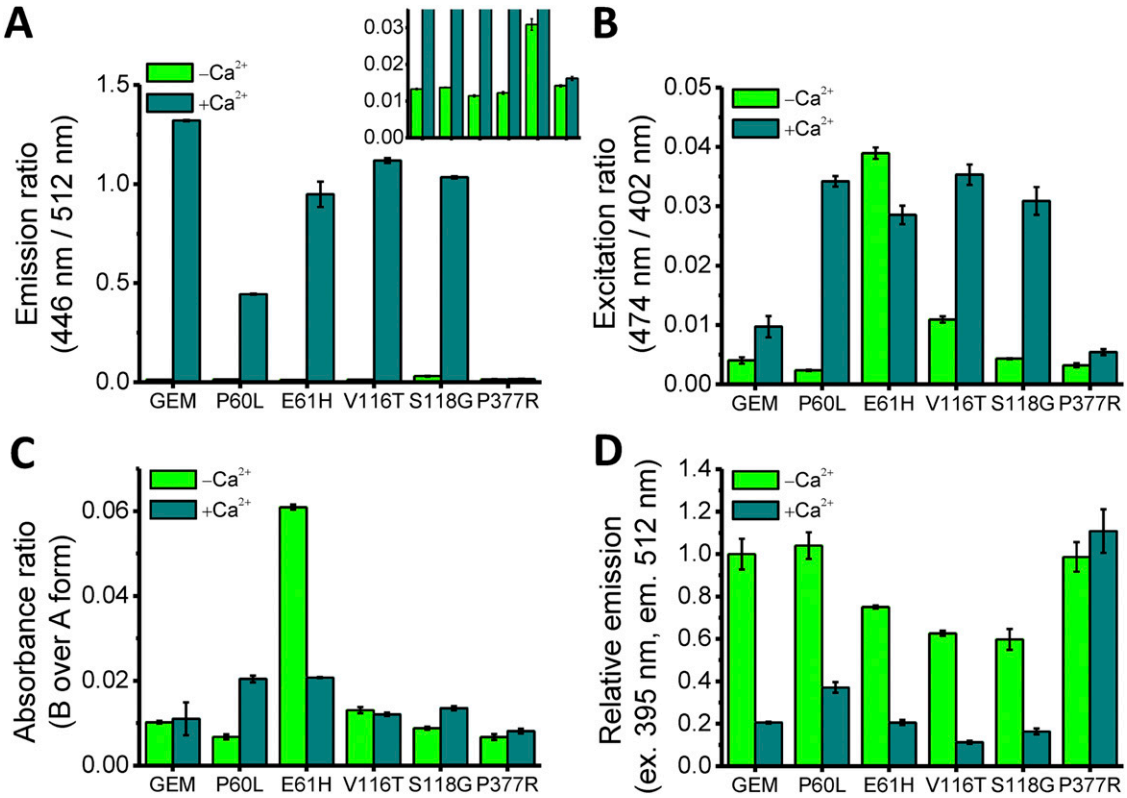

Fig. S6. Summary of fluorescence properties of GEM-GECO1 and its single-residue mutants. (*A*) Emission ratio of 446 nm over 512 nm with 395-nm excitation. *Inset* shows the enlarged plot. (*B*) Excitation ratio of 474 nm over 402 nm for 535-nm emission with and without Ca^{2+}. (*C*) Absorption ratio of the *B* form over *A* form. (*D*) Relative emission intensity at 512 nm with 395-nm excitation. The intensity was corrected by the absorbance at 395 nm. This process is dominated by ESPT.

Table S1. Kinetic data and mode assignments for excited-state peaks of GEM-GECO1

FSRS* (cm^{-1})	Calc.[†] (cm^{-1})	S_0 FSRS (cm^{-1})	Kinetics[‡] $-Ca^{2+}$	Kinetics[‡] $+Ca^{2+}$	Mode assignment (dominant motions)
819	818	814	(–) 1.1 ps (60%); 65 ps (40%)	(–) 1.8 ps (48%); 700 ps (52%)	Phenol ring breathing (1, 2, 3)[§]
885	874	855	(–) 1.1 ps (50%); 80 ps (50%)	(–) 1.2 ps (40%); 840 ps (60%)	Imidazolinone-ring deformation and C–C stretch plus bridge CH wagging (2, 3)
967	967[¶]	941	(–) 1.0 ps (62%); 40 ps (38%)	(–) 1.0 ps (60%); 680 ps (40%)	Phenol ring deformation (2, 3)
1,138 1,147[‖]	1,141	1,155 1,157[‖]	(–) 1.3 ps (50%); 42 ps (50%)	(–) 1.6 ps (55%); 837 ps (45%)	Ring H scissoring, bridge C–H rocking, and phenolic COH rock (1, 4)
1,180	1,178	1,174	(–) 730 fs (60%); 27 ps (40%)	(–) 630 fs (65%); 592 ps (35%)	Ring and bridge C–H rocking, phenolic COH rocking, and imidazolinone ring deformation (1, 4–6)
1,265	1,256	1,247 1,250[‖]	(–) 670 fs (64%); 34 ps (36%)	(–) 620 fs (62%); 468 ps (38%)	Phenolic C–O stretch (1, 4–6)
1,305 1,300[‖]	1,292	N/A	(–) 540 fs, (+) 31 ps, (–) 4.1 ns**	(–) 700 fs (60%); 472 ps (40%)	Bridge and phenol ring H rock with minor C–O stretch and COH rock (4, 6)
1,400	1,407	1,411	(–) 550 fs (60%); 41 ps (40%)	(–) 650 fs (70%); 840 ps (30%)	C–N stretch, bridge and phenol ring H rocking, small C = C stretching (5, 7)
1,446 1,442[‖]	1,449	1,455 1,452[‖]	(–) 675 fs (65%); 33 ps (35%)	(–) 740 fs (68%); 830 ps (32%)	C–N stretch, bridge and phenol ring H rocking, C–H and N–H wagging at the imidazolinone ring (1, 4, 7)
1,540	1,536[††]	N/A	(+) 28 ps; (–) 930 ps**	N/A	C = N and C–N stretch with a C = O (phenol) stretching component (1, 5, 6)
1,570 1,565[‖]	1,571	1,568 1,564[‖]	(–) 680 fs (61%); 36 ps (39%)	(–) 592 fs (58%); 900 ps (42%)	C = N stretch with some C = C stretching and C = O stretching motions (1, 4, 6, 7)

*The frequency is reported as an average of the mode frequencies from −100 fs to 1 ps to account for the spectral oscillatory behavior in the electronic excited state.

[†]The ES vibrational frequencies of a geometrically optimized neutral SYG chromophore were calculated with TD-DFT RB3LYP 6–31G+(d,p) in water (IEF-PCM-H_2O). The calculated frequencies are all with a scaling factor of 0.96.

[‡]A general observation is that in both Ca^{2+}-free and bound GEM-GECO1 samples the mode decay lengthens as the vibrational frequency decreases. The modes listed are primarily associated with A* state of the photoexcited neutral chromophore except the 1,305 and 1,540 cm^{-1} modes in the Ca^{2+}-free protein. For the 1,540 cm^{-1} mode, the rise time constant correlates with the A* → I* transition (ESPT process), whereas the decay time constant reports the energy relaxation of the I* state via fluorescence emission and/or other faster nonradiative processes.

[§]Representative literature that made similar normal mode assignment is listed.

[¶]This represents an averaged frequency of two calculated modes at ca. 959 and 975 cm^{-1} that both involve phenol ring deformation plus some minor C–N stretching motion.

[‖]The mode in the Ca^{2+}-bound protein.

**The rise component in these fits all starts at ∼4 ps, after which the I* mode dynamics dominate.

[††]Calculated from the optimized deprotonated chromophore at the same level of theory. This is a nascent I* mode.

1. Fang C, Frontiera RR, Tran R, Mathies RA (2009) Mapping GFP structure evolution during proton transfer with femtosecond Raman spectroscopy. *Nature* 462(7270):200–204.
2. Tozzini V, et al. (2003) The low frequency vibrational modes of green fluorescent proteins. *Chem Phys* 287(1–2):33–42.
3. Gnanasekaran R (2013) Normal modes and the Duschinsky mixing of the ground- and excited-state vibrations of the green fluorescent protein chromophore. *Chem Phys Lett* 587(0):61–67.
4. Schellenberg P, Johnson E, Esposito AP, Reid PJ, Parson WW (2001) Resonance Raman scattering by the green fluorescent protein and an analogue of its chromophore. *J Phys Chem B* 105(22):5316–5322.
5. Bell AF, He X, Wachter RM, Tonge PJ (2000) Probing the ground state structure of the green fluorescent protein chromophore using Raman spectroscopy. *Biochemistry* 39(15):4423–4431.
6. He X, Bell AF, Tonge PJ (2002) Isotopic labeling and normal-mode analysis of a model green fluorescent protein chromophore. *J Phys Chem B* 106(23):6056–6066.
7. Esposito AP, Schellenberg P, Parson WW, Reid PJ (2001) Vibrational spectroscopy and mode assignments for an analog of the green fluorescent protein chromophore. *J Mol Struct* 569(1–3):25–41.

Table S2. Ground-state Raman peak assignments for GEM-GECO1 $\pm Ca^{2+}$

FSRS in ground state S_0 (cm^{-1})	Calculated* (cm^{-1})	Mode assignment (dominant motions)
814	813	Phenol ring breathing
855	851	Imidazolinone ring deformation with minor phenol ring deformation
904	908	Phenol ring asymmetric HOOP† and bridge C–H wagging
941	939	Phenol ring HOOP
960	951	Phenol ring asymmetric HOOP
1,041	1,049‡	Imidazolinone ring deformation and C–H wags
1,100	1,085	Phenolic COH rocking, ring-H scissoring and some phenol ring breathing
1,125	1,128	Phenol ring COH rocking, ring-H scissoring, bridge C–H rocking
1,155/1,157§	1,156	Strong phenol ring COH rocking, ring-H scissoring, bridge C–H rocking, and some imidazolinone ring deformation
1,174	1,185	Delocalized phenol-H rocking, bridge C–H rocking, and imidazolinone deformation plus some sidechain motion
1,209	1,216	Phenol ring-H rocking, bridge C–H rocking, and imidazolinone ring C–C stretching
1,247/1,250§	1,241	Strong phenol C–O stretch with some ring-H rocking
1,322/1,320§	1,322	Phenolic COH rocking, ring-H rocking, bridge C–H rocking, and phenol ring deformation
1,343	1,347	Bridge C–H rocking (strong) with imidazolinone C–N stretching and phenolic COH rocking components
1,411	1,412	Phenolic and imidazolinone C = C, C–C and C–N stretching, phenolic COH rocking, bridge C–H rocking
1,455/1,452§	1,453	Imidazolinone deformation and sidechain N–H wags
1,568/1,564§	1,570	Imidazolinone C = N stretching with phenolic C = C stretching

*The ground-state Raman frequencies were calculated from an optimized SYG chromophore capped with methyl groups with DFT RB3LYP 6–31G+(d,p) in water (IEF-PCM-H_2O). All of the calculated frequencies are with a scaling factor of 0.96.
†HOOP stands for hydrogen out-of-plane motion.
‡This represents an averaged frequency of the two calculated modes at ca. 1028 and 1070 cm^{-1} that both involve imidazolinone ring deformation with some minor C–H wagging motion.
§The vibrational mode frequency in the Ca^{2+}-bound GEM-GECO1 protein.

Table S3. Functional residues in wtGFP (1) and GEM-GECO1 (2–5) representative structures from PDB

wtGFP residues (2WUR)	GEM-GECO1 residues (3SG3/3EKJ/3EVR)
S65-Y66-G67 (chromophore)	S223-Y224-G225 (chromophore)
H148	No residue at this position. R377 in GCaMP is functionally equivalent; L60 and E61 are most similar in position. However, GEM-GECO1 has R377P and L60P mutations (*SI Text*).
T203	V116
S205 and E222	S118 and E135

The relevant GCaMP crystal structures are used to represent GEM-GECO1 because no crystal structure is available for the latter protein. The GCaMP3 structure 3SG3 has V116, whereas the GCaMP2 structures (3EKJ/3EVR) have T116. All of them have a TYG chromophore.

1. Shinobu A, Palm GJ, Schierbeek AJ, Agmon N (2010) Visualizing proton antenna in a high-resolution green fluorescent protein structure. *J Am Chem Soc* 132(32):11093–11102.
2. Zhao Y, et al. (2011) An expanded palette of genetically encoded Ca^{2+} indicators. *Science* 333(6051):1888–1891.
3. Akerboom J, et al. (2009) Crystal structures of the GCaMP calcium sensor reveal the mechanism of fluorescence signal change and aid rational design. *J Biol Chem* 284(10):6455–6464.
4. Wang Q, Shui B, Kotlikoff MI, Sondermann H (2008) Structural basis for calcium sensing by GCaMP2. *Structure* 16(12):1817–1827.
5. Leder L, et al. (2010) The structure of Ca^{2+} sensor Case16 reveals the mechanism of reaction to low Ca^{2+} concentrations. *Sensors (Basel)* 10(9):8143–8160.

Table S4. Oligonucleotides used for GEM-GECO1 site-specific mutagenesis

Mutation	Sequence
P60L	aggtcggctgagctcactagagaacgtgtatataa
E61H	ggtcggctgagctcaccacataacgtgtatataaaggcc
V116T	ccgacaaccactacctgagcacccagtccatactttcgaaaga
S118G	cactacctgagcgtgcagggcatactttcgaaagaccc
P377R	ttcctgacaatgatggcacgcaaaatgcaggacacagaca